

EEG 92154

High resolution EEG: 124-channel recording, spatial deblurring and MRI integration methods

Alan Gevins *, Jian Le, Nancy K. Martin, Paul Brickett, John Desmond and Bryan Reutter

EEG Systems Laboratory and Sam Technology, 51 Federal Street, San Francisco, CA 94107 (USA)

(Accepted for publication: 27 November 1993)

Summary This paper describes a method for increasing the spatial detail of the EEG and for integrating physiological data with anatomical models based on magnetic resonance images (MRIs). This method includes techniques to efficiently record EEG data from up to 124 channels, to measure 3-D electrode positions for alignment with MRI-derived head models, and to estimate potentials near the outer convexity of the cortex using a spatial deblurring technique which uses a realistic model of the structure of the head and which makes no assumptions about the number or type of generator sources. The validity of this approach has been initially tested by comparing estimated cortical potentials with those measured with subdural grid recordings from two neurosurgical patients. The method is illustrated with somatosensory steady-state evoked potential data recorded from 5 healthy subjects. Results suggest that deblurred 124-channel topographic maps, registered with a subject's MRI and rendered in 3 dimensions, provide better spatial detail than has heretofore been obtained with scalp EEG recordings. The results also suggest that the potential for EEG as a functional neuroimaging modality has yet to be fully realized.

Key words: 124-Channel EEG; Spatial deblurring; Magnetic resonance image; Finite element method; Functional localization; Steady-state evoked potentials

In comparison with other techniques for imaging brain function, the scalp EEG as traditionally recorded and analyzed has unsurpassed temporal resolution, but, at best, modest spatial resolution. The low spatial detail provided by the standard EEG derives in part from the fact that the topography of a brain electrical field is distorted or blurred as it is volume conducted through the skull and other tissues. This report documents our recent efforts to minimize such blurring effects, and to integrate high-resolution topographic evoked potential maps with 3-dimensional structural models of the head and brain surface derived from magnetic resonance images (MRIs). The progress described in this communication suggests that it is realistic to anticipate the advent of a hybrid modality for functional neuroimaging capable of providing: (1) millisecond temporal resolution of neurophysiological function with a useful degree of spatial detail of elec-

trical fields roughly approximating that obtained with direct recordings from superficial cortical regions; (2) 1–2 sec temporal resolution of metabolic function with good 3-dimensional resolution using functional MRI (Belliveau et al. 1991; Ogawa et al. 1992, 1993); and (3) excellent anatomical detail derived from the integration of physiological data with MRI-derived structural renderings.

In order to improve EEG spatial resolution, it is first necessary to sample the topography of brain electrical events at a density sufficient to accurately reflect those events. With the standard 19-site recording montage of the international 10–20 system (Jasper 1958), the typical distance between electrodes on an average adult male head is about 6 cm. Because of the blurring effects of volume conduction, it has often been assumed that these 19 sites provide enough spatial sampling to capture all the meaningful topographic detail afforded by the scalp EEG. However, it is becoming clear that, in principle, additional non-redundant information can often be obtained by recording from an increased number of electrodes (Lehmann 1986; Gevins

* Corresponding author. Tel.: (415) 957-1600, ext 133; Fax: (415) 546-7121.

1988, 1990). For example, the 3 dB point of the point spread function for conductance of potentials from the brain surface to the scalp averages about 2.5 cm (Gevins 1987, 1990). This level of spatial detail is undersampled even with 64 electrodes, which provide an average inter-electrode distance of about 3.3 cm. With 128 electrodes, an average inter-electrode distance of roughly 2.25 cm can be obtained. Although this sampling density is still insufficient to resolve the topography of punctate sources, it likely provides an adequate representation of the scalp topography of most brain electrical events of interest to researchers and clinical practitioners. We have thus sought to refine practical methods for making simultaneous scalp recordings from upwards of 100 electrodes.

In addition to recording from a large number of electrodes, the approach employed here for deriving "high resolution EEGs" also involves minimizing the blur distortion observed in scalp EEG recordings. The deblurring of scalp potentials is accomplished by estimating cortical potentials utilizing a realistic finite element model of the subject's head. This finite element model is constructed from anatomical information regarding local scalp and skull thickness derived from MRIs. Three-dimensional locations of electrode sites and fiducial skull landmarks are measured and aligned with the realistic head model. Then, scalp data are registered with the head model using the EEG-MRI alignment, and cortical potentials are estimated based on this realistic finite element model of electrical conduction through the scalp and skull tissues (Le and Gevins 1993). Finally, 3-dimensional graphical visualization tools are utilized to examine the spatially enhanced results. In what follows, these techniques are described in detail and applied to the analysis of steady-state somatosensory evoked potentials elicited in healthy subjects by electrical stimulation. Further, we document our initial attempts to validate the deblurring procedure by comparing the distribution of electrical fields at the cortical surface as calculated from high resolution scalp recordings in epileptic patients with those obtained via direct recordings from subdural electrode grids in these same patients.

Methods

(A) EEG recording

Subjects

Seven clinically healthy right handed male subjects (ages 21–34 years) and 2 female neurosurgical patients (ages 20 and 21 years) took part in this study. Two additional healthy subjects participated in pilot record-

ings during which the methods were developed and refined. All participation was fully informed and voluntary.

Somatosensory stimulation protocol

Steady-state somatosensory evoked potentials (SEPs) were elicited by electrical stimulation delivered to the finger at a rate of 14.92 Hz using 0.2 msec electrical pulses generated by a Grass S11 stimulator. Grass bipolar electrodes were affixed to the palmar surface of the proximal interphalangeal joint. For healthy subjects, the right index finger and right and left middle fingers were stimulated individually. For neurosurgical patients, all 5 fingers of the right hand were stimulated separately. Stimuli were presented to each finger in 100 sec segments for a total of 300 sec. In each 100 sec segment, 0–12 stimuli were randomly omitted, and the subject was instructed to count the number of omitted stimuli and to report this number at the end of each 100 sec block. Feedback regarding accuracy of omitted stimulus detection was reported to the subject after each block. The stimulus intensity was set by the subject so individual pulses were perceived without pain. Data collected for two of the healthy subjects were eliminated from further analyses because they set the stimulus intensity at a level that was too low to produce an acceptable *signal-to-noise* ratio.

Data collection system and scalp and cortical grid recording protocols

For scalp recordings, 2 sets of 64-channel Bioelectric Instrument amplifiers were used to record physiological signals (EEG and EOG) with a bandpass of 0.5–50 Hz. The bandpass was adjusted to 0.5–100 Hz for neurosurgical patients to match filter settings used in cortical grid recordings. Data acquisition was done using two computers, a Concurrent 5700 running a real-time UNIX operating system, and an IBM PC-compatible 386 running DOS. The PC presented stimuli to the subject and controlled data collection by the Concurrent, which also displayed several (operator-specified) wave forms in real time. In addition, gross artifacts from eye blinks or other eye movements, and saturated or dead electrodes were detected on-line and color-coded in the display. Before each recording session, a calibration procedure was performed in which an 80 μ V square-wave signal was recorded, and the calculated gain was used to equalize all channels. Data were recorded at 128 samples/sec for healthy subjects and at 256 samples/sec for neurosurgical patients for 100 sec stimulation runs. Calibrated data with other event-timing information were written to hard disk in a format-including Data Description Language. Additional features of this system have been described elsewhere (Gevins et al. 1990). For cortical grid record-

ings on neurosurgical patients, one set of 64-channel MICROSAM amplifiers (BMSI) was used to record ECoG signals with a bandpass of 0.5–80 Hz and a digitization rate of 240 samples/sec.

Healthy subjects and neurosurgical patients participated in one recording session in which EEG was recorded from 124 scalp electrodes. In each such recording, the subject was seated in a sound-attenuated, electrically shielded room. Following adjustment of electrical stimulus intensity levels, 3 somatosensory stimulation conditions were performed, each for 100 sec. For normal subjects, sets of somatosensory stimulation conditions were followed by stimulation conditions in other modalities, and the entire sequence of stimulation conditions was repeated 3 times in the same order. Only somatosensory stimulation was presented to neurosurgical patients. Neurosurgical patients participated in a second recording session in which steady-state SEPs were collected from a 64-channel cortical grid which was implanted after a craniotomy was performed. The results from somatosensory stimulation conditions are described herein.

Electrode system and 3-D position measurement

In order to make the application of a large number of EEG electrodes more practical, electrode hats were custom made from stretchable fabric and commercial tin-disk electrodes encased in plastic holders. The hat used in the present study was positioned on the head by reference to the nasion,inion and preauricular notches and stretched so that the vertex electrode was positioned correctly. Individual scalp sites were cleaned and abraded through the hole in the top of each electrode, and conducting gel was injected. This procedure was repeated whenever electrical impedance was above 5000 Ω . Other electrodes were attached with surgical tape over the left and right mastoids (right mastoid used as reference; left mastoid recorded for latter referencing by averaged mastoid), the outer canthi (for horizontal electrooculogram, EOG), and on the sub- and supraorbital ridges of the right eye for vertical EOG. Alternative ground electrodes were attached to the forehead and to both wrists which were also wrapped with gauze strips soaked in electrode gel. Application of the EEG and other electrodes took 3 research assistants about 90 min to complete.

After application of the electrode hat, the 3-D coordinates of each electrode position were measured with a Polhemus magnetic digitizer that has coils which sense the 3-dimensional position of the probe tip with respect to a magnetic field source. The magnetic field source was attached to a head support device, which was used to keep the subject's head stationary with respect to the magnetic field source during digitization

of electrode positions. Measurements were also made of the skull landmarks used in the 10/20 system, i.e., the nasion,inion, and preauricular notches. These coordinates were used to align the electrode positions with MRI-derived head models. A graphical interface was developed to select the electrodes to be measured and to display the digitized position of each electrode on a 2-dimensional projection of the head. Position measurement was accurate to better than 3 mm (RMS).

A standard nomenclature for defining electrode placements additional to the original 19 placements of the international 10–20 system (Jasper 1958) has been adopted by the American Electroencephalographic Society (Sharbrough et al. 1990). The basic idea in this and other systems used previously (Gevins 1988, 1989) is to add electrodes so that all of the 10% locations are covered above the circumference line through the Fpz and Oz electrodes and to extend additional rows at 10% spacing inferior to electrodes on the circumference line. This yields 61 electrode locations at or above the circumference line. In the system used at our laboratory, any arbitrary position is described by appending 2 additional numbers to the electrode name. These numbers indicate the proportional distance to the next anterior and medial 10% electrode position, respectively. To keep names to a minimum length and still allow arbitrary precision, the decimal point is omitted and both of the appended numbers are required to have the same number of digits. For example, in the standard system electrode AF3 is 10% anterior of F3, and F3 is 10% medial of F5. Therefore, an electrode halfway between F5 and AF3 would be named F555 (i.e., F5[0.5][0.5]), while an electrode one quarter of the distance from F5 to F3 would be named F50025 (F5[0.00][0.25]). The 124-channel montage we have used yields 101 channels above the circumference line.

(B) MRI data processing

MRI analysis and anatomical modeling

MRIs for all subjects were acquired with an MR imager operating at 1.5 Tesla. Three healthy subjects (subjects 1, 4, 5) were scanned with a General Electric Signa scanner (Sequoia Hospital, Redwood City, CA) to obtain T1-weighted contiguous 3 mm thick horizontal slices with an in-plane resolution of ~ 1.2 mm (2-D spin echo, TR = 600, TE = 20). Two healthy subjects (subjects 2, 3) were scanned with a Siemens Magnetom scanner (Veterans Administration Medical Center, San Francisco, CA) in 3-D acquisition mode to obtain T1-weighted contiguous 1.5 mm by 1 mm by 1 mm voxels (subject 2: MP RAGE, TR = 10, TE = 4, 10° flip; subject 3: 3-D FLASH, TR = 30, TE = 5, 40° flip). Neurosurgical patients were scanned with a General Electric

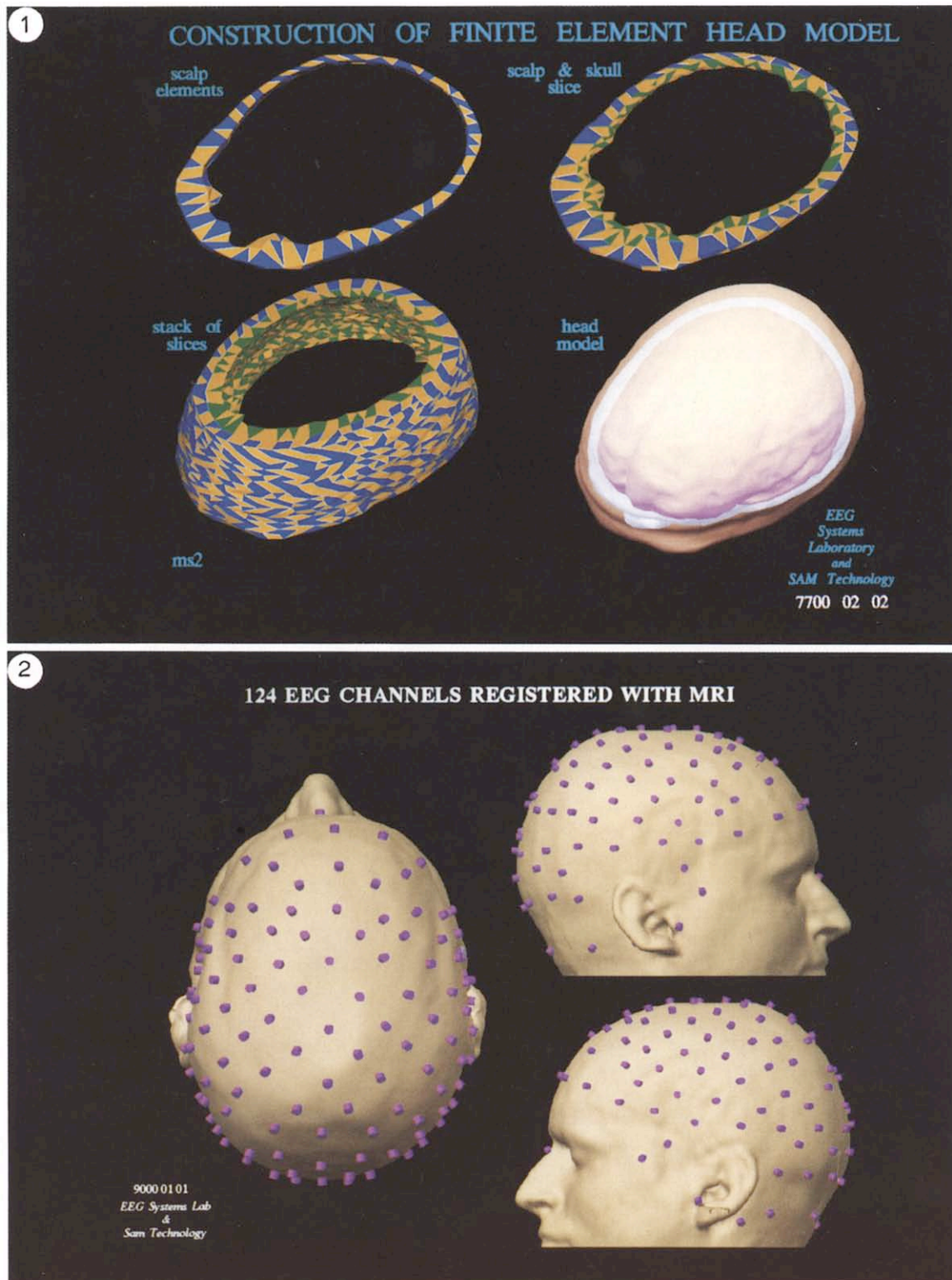


Fig. 1. Construction of a finite element model of scalp and skull volumes. The upper left shows a single ring of scalp elements with alternating scalp elements shown in blue and yellow. The upper right shows the addition of skull elements, alternating in green and yellow for a single slice bounded by two consecutive horizontal MR images. The lower left shows all slices except for the topmost horizontal slice. The lower right shows the scalp, skull and brain surfaces rendered as transparent.

Fig. 2. Graphic display of EEG-MRI alignment. Three views of the scalp surface reconstructed from the subject's MRI are shown with small disks on the surface of the scalp representing electrode positions. Disks over nasion and preauricular notches represent fiducial points which were used in the alignment procedure.

Signa scanner (University of California Medical Center, San Francisco, CA). T1-weighted contiguous 3 mm thick horizontal slices with an in-plane resolution of ~ 1.1 mm (2-D spin echo, TR = 600, TE = 20) were obtained for patient 1. T2-weighted non-contiguous 5 mm thick clinical horizontal slices with an in-plane resolution of ~ 0.9 mm and an inter-slice gap of 2.5 mm (2-D spin echo, TR = 2600, TE = 30) were obtained for patient 2.

Data conversion routines were written to read MRI data tapes and to write a file for each image containing the data format, the image data, and associated 3-D image geometry information (i.e., location and voxel dimensions) for subsequent modeling. Processing of each subject's MRI involved contouring the scalp, skull, and cortical layers on each MRI slice for use in constructing a finite element model of the head tissues and in the alignment of EEG and MRI data in a common 3-D coordinate system. Analysis tools were developed to process these data since the commercial software currently available which provides for 3-D visualization from MRIs does not provide algorithms for volume modeling that are suitable for our needs.

Contouring, surface construction and rendering

Automated contouring of individual MR images was developed to construct a triangular surface mesh of the scalp which was used for electrode alignment and 3-D mapping of evoked potentials (Gevins 1989; Gevins et al. 1990). Each individual horizontal image was viewed on a graphics screen by an operator who could interactively set the starting point and threshold level, and manually edit each contour if necessary. For patient 1, every other image over the top half of the head had to be discarded because of a head movement, yielding contours spaced 6 mm apart in this region. For patient 2, adjacent images were interpolated using a spatially varying "morphing" operation. The original and interpolated images were then processed, yielding contours spaced 3.75 mm apart. The resulting set of contours were triangularized to form a continuous surface model. These surface models were then rendered using our programs (and most recently, programs by Silicon Graphics, Inc.) for 3-D graphics. For display of potentials mapped onto the scalp or cortical surfaces, a color palette was created to represent the positive through negative range of values, with white indicating zero.

Construction of finite element models

A finite element model of the realistic scalp and skull volumes was created from each subject's MRIs. The scalp and skull volumes in the model were composed of a set of tetrahedral finite elements. Because of the necessity for a regular arrangement of vertex

points for the finite elements, and the difficulty in identifying the cortical surface automatically, a manual contour method was implemented for generating the finite elements which delimited the scalp, skull and cortical surfaces.

Horizontal contours which delineate the scalp/exterior border, the skull/scalp border, and the brain/skull border were created. Sixty-four radial lines emanating from the center of the head were superimposed on each MR image to guide visual placement of contour points in order to assure consistent inter-point spacing. Finite elements were automatically constructed from the contours as follows. For each point on a given contour for a given MRI slice, edges were formed between that point and: (a) adjacent points on the same contour for the same slice, (b) the homologous point and the next point lying on an adjacent contour of the same slice, (c) the homologous point and the next point lying on the same contour of an adjacent slice, and (d) the homologous point and the next point lying on an adjacent contour of an adjacent slice. Triangular faces were formed from the edges and tetrahedrons were formed from the faces. These tetrahedrons, which partitioned the entire volume, constituted the finite elements (Fig. 1). The finite element construction procedure has been recently improved by an additional regularization step in which vectors from a central origin are used to locate radially superimposed points on the scalp, skull, and cortical surfaces defined by the original finite elements. These points formed the vertices of triangular prisms which were then divided into tetrahedral finite elements for deblurring (to be defined in the following section). The cortical surface models shown in the Results section consist of the innermost triangular faces of the original tetrahedral elements, onto which the deblurred potentials have been interpolated.

EEG electrode-MRI alignment

In order to transform the digitized electrode positions into the same coordinate system as the MR images, translation in the x, y and z directions and rotation about the x, y and z axes must be estimated and performed. This has been done in two ways, using either an automatic iterative method or an interactive manual method. The automatic iterative method can be used when the alignment is reasonably close to start with or has been visually adjusted. The average distance from each electrode to the nearest point on the MRI-derived scalp surface is found first, and then the 6 transformation parameters are adjusted to minimize this value using the Simplex method, a non-linear optimization algorithm (Nelder and Mead 1965). The manual EEG-MRI alignment procedure which we have implemented utilizes digitized skull landmarks (the na-

sion, theinion, the vertex and preauricular points) to construct a pyramid which is manually aligned with the corresponding MRI-based scalp surface landmark using 3-D graphics software (Silicon Graphics, Inc.) which allows for easy 3-D transformation using a mouse as a "virtual trackball." The resulting transformation is then used to transform the entire set of electrodes into the MRI coordinate system, and the transformed electrode positions are "snapped" to the MRI scalp surface. Fig. 2 shows an example of the electrode positions aligned with and snapped to the MRI-derived scalp surface.

(C) spatial enhancement with finite element deblurring

Finite element deblurring (also called deblurring) is a mathematical spatial enhancement procedure which uses an MRI-derived anatomically realistic model of the passive conducting properties of each subject's head and a finite element model to estimate potentials at the cortical surface from scalp potentials (Gevins et al. 1991; Le and Gevins 1993). Unlike other methods which estimate cortical potentials or currents (e.g. Nicholas and Deloche 1976; Freeman 1980; Hill et al. 1988; Sidman et al. 1989, 1992), Deblurring is a true "downward continuation" method in that the cortical potential distribution is derived without prior knowledge or assumptions about the generating sources. Also, deblurring uses a realistic model of the head shape and local tissue thicknesses, rather than assuming that the scalp, skull and brain are spherically shaped.

Deblurring calculations are based on an application of Poisson's equation which describes the potential distribution in the skull and scalp layers,

$$\nabla \cdot (\sigma(x, y, z) \nabla u(x, y, z)) = F(x, y, z) \equiv 0, \quad (1)$$

where $\sigma(x, y, z)$ is the conductivity tensor, $u(x, y, z)$ is the potential distribution function and $F(x, y, z)$ is the source function within the head. $F(x, y, z)$ is zero within the scalp and skull layers because these two layers contain no generating sources. The boundary condition on the scalp surface is

$$\sigma \nabla u(x, y, z) \cdot \mathbf{n} = 0, \quad (2)$$

where \mathbf{n} is the normal direction vector, since electric current does not flow out of the scalp surface into the air. The additional boundary condition on the cortical surface and the bottom surface of the modeled scalp and skull volumes is

$$u(x, y, z) = G(x, y, z), \quad (3)$$

where $G(x, y, z)$ is a potential distribution function.

For deblurring calculations, the finite element method is applied to a conducting model composed of

tetrahedral elements to find a numerical forward solution $u(x, y, z)$ of Eq. (1) with boundary conditions specified in Eqs. (2) and (3) (Strang and Fix 1973). A sparse solver is used to find the initial numerical cortical potential distribution function $G(x, y, z)$. Then a multidimensional optimization scheme is employed that searches for an optimal cortical potential map whose numerical forward solution best fits the given measured scalp potential data.

Prior to application of the finite element method, the potentials measured at the electrode positions are interpolated onto vertices of tetrahedrons defining the scalp model using a local spline-like interpolation function which is active near the area of interest and dormant outside this region (Le and Gevins 1993). These interpolated potential measurements at the scalp are compared with the numerical forward solution at each step of the deblurring procedure.

After deblurring, the resulting potentials are low-pass filtered to eliminate spatial frequencies higher than those which can be resolved with the spatial sampling set by the interelectrode spacing on the scalp. The spatial smoothing of samples of an estimated cortical potential function $u(x, y, z)$ obtained at the finite element vertices $\mathbf{p}_i = (x_i, y_i, z_i)$, $i = 1, \dots, n$, on the cortical surface is accomplished by using the spatially varying Gaussian low-pass filter

$$u(\mathbf{p}) = \frac{\sum_{i=1}^n U(\mathbf{p}_i) e^{-|\mathbf{p}-\mathbf{p}_i|^2/2\sigma^2} \prod \left(\frac{|\mathbf{p}-\mathbf{p}_i|}{2k\sigma} \right)}{\sum_{i=1}^n e^{-|\mathbf{p}-\mathbf{p}_i|^2/2\sigma^2} \prod \left(\frac{|\mathbf{p}-\mathbf{p}_i|}{2k\sigma} \right)}, \quad (4)$$

where

$$\prod(\alpha) = \begin{cases} 1, & -1/2 \leq \alpha \leq 1/2 \\ 0, & \text{else.} \end{cases}$$

The rectangle function $\prod(|\mathbf{p}-\mathbf{p}_i|/(2k\sigma))$ is used to truncate the Gaussian $e^{-|\mathbf{p}-\mathbf{p}_i|^2/2\sigma^2}$ for $|\mathbf{p}-\mathbf{p}_i| > k\sigma$, where k is 3 and σ is 0.75.

The improved spatial detail obtained by deblurring is limited by the fact that deblurring is an inverse filter function. The Deblurring procedure acts as a high-pass filter, and because of this property, instabilities may result due to high spatial frequencies associated with the presence of noise. If high spatial frequency noise is present, an appropriate spatial filter function may be applied to the scalp data prior to deblurring to minimize these instabilities. Since the effects of spatial noise and spatial pre-filtering on deblurring are currently under investigation, the data presented herein were not spatially prefiltered prior to deblurring.

Results

(A) Harmonic analysis of the steady-state EP signal

Steady-state EPs are repetitive signals which have discrete frequency components that remain relatively constant in amplitude and phase. Therefore the signal power is concentrated in narrow frequency bands that are centered at the fundamental and harmonic frequencies of the eliciting stimulus (Regan 1972, 1989). In contrast, biological "noise" (activity unrelated to the stimulus) is distributed throughout the frequency spectra. Given that the frequency domain characteristics of the 14.92 Hz steady-state SEP signals were known, it was possible to apply a frequency extraction procedure to the data to enhance the SNR of the recorded SEP signals. This method consists of 4 steps: data averaging, Fourier transform, frequency extraction, and inverse Fourier transform (Nakamura et al. 1989). For each

stimulus condition, artifact-free epochs of 0.53125 sec were averaged and digitally re-referenced to the "average mastoid" by subtracting one-half of the left mastoid amplitude at each time point from all other channels. After application of a Hanning window, the Discrete Fourier Transform (DFT) was computed, and the real and imaginary spectral amplitude values were extracted for all components harmonically related to the stimulation frequency. Since the recording bandpass was set from 0.5 to 50 Hz, only the first 3 harmonics were extracted. Non-harmonic frequency bins were zeroed, and the inverse DFT was applied to each block, effectively rejecting the noise that was not harmonically related to the steady-state signal.

Fig. 3a illustrates an average of 179 epochs (0.53125 sec in duration) of 14.92 Hz steady-state response to electrical stimulation of the right index finger recorded at channel AC355 for one healthy subject. Approximately 8 stimulus cycles are displayed over 0.53125 sec.

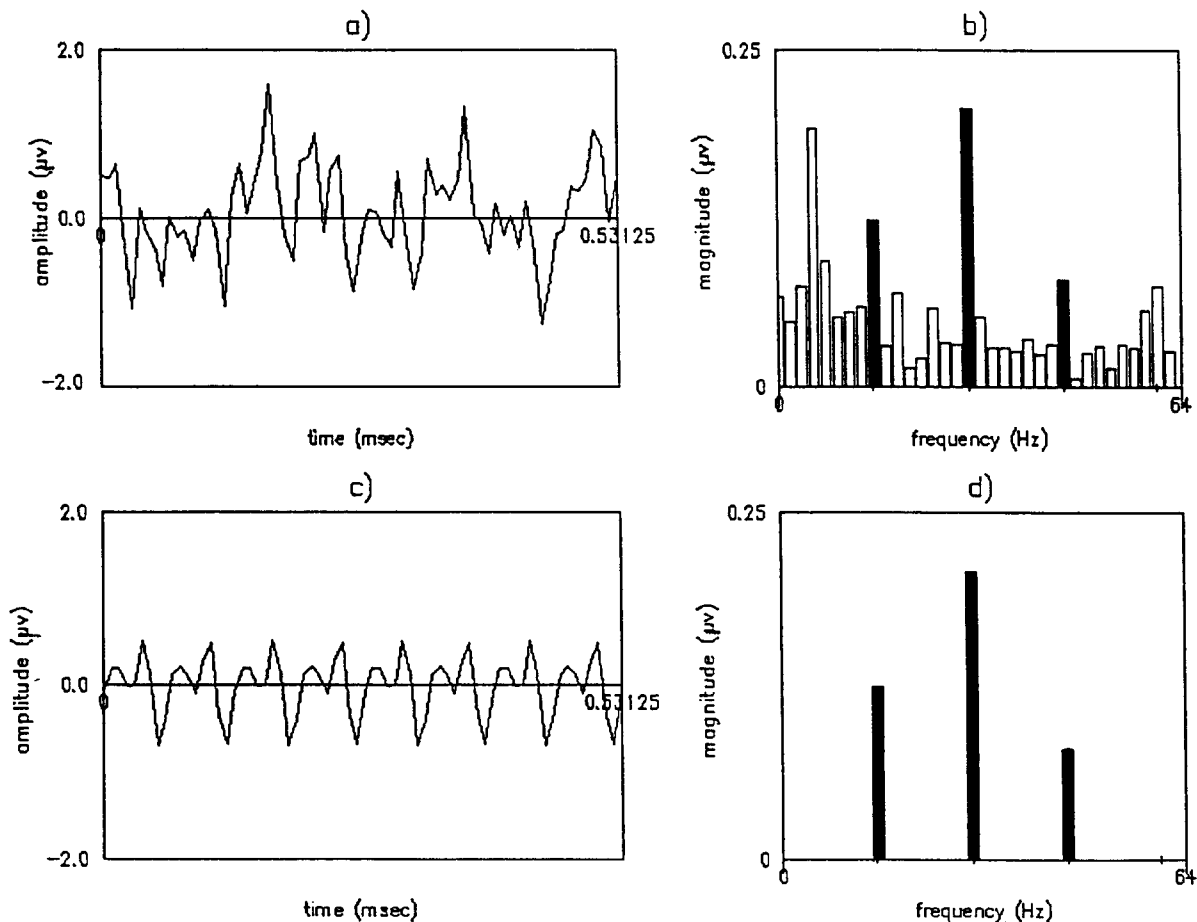


Fig. 3. Harmonic analysis of steady-state somatosensory evoked potentials of subject 1. a: the average of 179, 0.53125 sec, epochs of steady-state signals in response to electrical stimulation of the right index finger recorded at channel AC355. b: the frequency domain representation of the same averaged time series. The frequency components at which the response may occur are shaded. c: the time series recovered by the frequency extraction method including only those frequencies at which the response may occur. d: the response frequency components.

Fig. 3b illustrates the frequency domain representation of this time series. The fundamental and harmonic frequency components at which the response may occur have been shaded. The power of the 14.92 Hz steady-state SEP time series is concentrated in the harmonic frequency bands illustrated in Fig. 3d, with most of the energy in the fundamental and second harmonic bins. Fig. 3c shows the response after the frequency extraction method has been applied. By including only frequencies at which the response may occur, much of the noise in the time series is eliminated. Fig. 4 illustrates the average of 14.92 Hz steady-state responses to electrical stimulation of the right index finger at 119 channels over a 0.262 sec interval for 3 blocks recorded from the same subject illustrated in Fig. 3. Fig. 5 illustrates the same data after the harmonic frequency extraction method has been applied. Although the steady-state SEP amplitude elicited at 14.92 Hz was small ($0.61 \mu\text{V}$) in comparison to SEPs elicited at lower stimulation frequencies (Delberghe et al. 1990; Snyder 1992), this procedure made it possible to obtain good separation of the steady-state signal from noise.

The steady-state SEPs recorded from the 5 healthy subjects in this study were processed using the frequency extraction method, and the resulting responses are shown in Fig. 6. The left column contains the left middle finger responses, the middle column illustrates the right middle finger responses, and the right column shows right index finger responses for the channel exhibiting the largest peak amplitude and its homologous channel over the opposite hemisphere. Global energy was computed at 1° intervals within the steady-state cycle as the square of the potentials summed over all channels. A vertical line was placed at the phase at which the maximal global energy occurred. This phase varied between subjects and conditions.

Spatial potential maps were extracted at the maximal energy phase. Fig. 7 illustrates conventional 2-D topographical maps of 124-channel steady-state SEPs in 3 conditions at the maximal energy phase for each subject. The scalp potential magnitudes illustrated in this figure ranged from 0.56 to $1.24 \mu\text{V}$, which are consistent with those elicited by mechanical finger stimulation at 17 Hz (Snyder 1992). They are also consistent with other findings that the amplitude of SEP components decreases as the stimulation frequency increases (Namerow et al. 1974; Pratt et al. 1980; Delberghe et al. 1990; Snyder 1992), and that

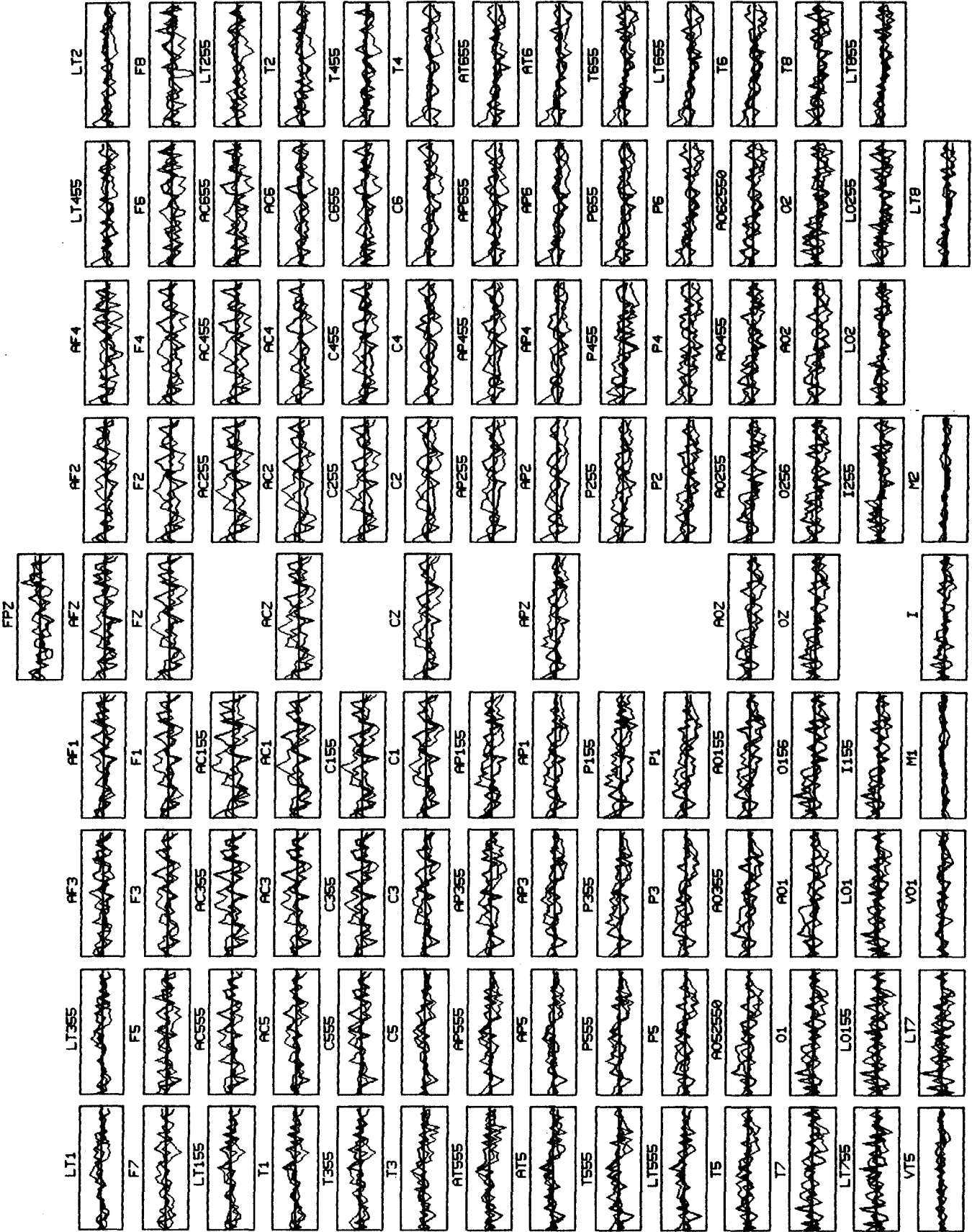
electrical stimulation of a finger produces a smaller response than electrical stimulation of the median or ulnar nerve (Desmedt and Brunko 1980). The somatosensory responses for all 5 subjects exhibited the expected maximal activity in the hemisphere contralateral to the finger stimulated (cf., Lüders et al. 1986). Utilizing maximal energy as the criterion for phase selection resulted in some between-subject differences in the phase selected for topographic mapping. As a result, the topographies for the right index finger response for subject 3 and the right and left middle finger responses for subject 1 exhibit a polarity inversion opposite that in the other maps.

(B) Spatial enhancement

Deblurring was performed on data obtained with the frequency extraction method (illustrated in Fig. 7) for each individual subject. Because of the considerable anatomical differences between subjects evident in their MRIs as well as individual variability in their EPs and their phase of maximum energy, data for each subject and each stimulus condition are presented here. Figs. 8 and 9 illustrate the original scalp and deblurred potentials for 3 somatosensory stimulation conditions for subjects 2 and 3, respectively. A coarse image of each subject's cortical anatomy (obtained by stacking consecutive horizontal MRI images) is also displayed in order to relate deblurred cortical potentials with individual cortical landmarks. Attempts have been made to delimit the pre- and post-central gyral regions in the stacked MR images. A yellow box is drawn around this region, and a black line approximating the individual's central sulcus is superimposed on the deblurred images.

The scalp potential magnitudes (illustrated in these figures) ranged from 0.56 to $0.94 \mu\text{V}$. For both subjects, the scalp potentials show polarity inversions contralateral to the stimulated finger, but exhibit less spatial detail than the deblurred potentials. The maximum and minimum deblurred potentials are situated on either side of the central sulcus, which is consistent with a tangential generator situated within the posterior bank of the central sulcus (Allison 1987; Allison et al. 1989a,b). The deblurred cortical potentials displayed in Figs. 8 and 9 were computed using the textbook value of 80 for the scalp/skull conductivity ratio. Since the exact conductivity values for individual subjects are not available, deblurring calculations were

Fig. 4. Three averages, each with ~ 179 , 0.53125 sec. trials of 14.92 Hz steady-state responses evoked by electrical stimulation of the right index finger as recorded at 119 channels for subject 1. A 0.262 msec interval is illustrated containing approximately 4 cycles of the steady-state evoked response.



also performed using conductivity ratios of 40, 120, and 160. Results showed that different conductivity ratios produced gradual differences in the topographic maps but did not affect the general pattern or location of the potential maxima (Le and Gevins 1993). As one would expect, higher conductivity ratios produced larger cortical potential values. Therefore, when different conductivity ratios were used, differences in magnitudes of the estimated cortical potentials were produced. For example, when the scalp potential data for the left middle finger response for subject 2 (Fig. 8, left column) was deblurred using conductivity ratios of 40, 80, 120, and 160, the maximum cortical potential value calculated was 5.56, 10.23, 14.89 and 19.56 μV , respectively. There was no difference in general patterns among the same set of cortical maps.

The cortical anatomy and deblurred potentials for 3 somatosensory stimulation conditions are illustrated in Fig. 10 for subjects 1, 4, and 5. In each row, the left middle finger response, right middle finger response and right index finger response are illustrated for an individual subject. The deblurred potentials for subjects 1 and 5 exhibit a polarity inversion across the central sulcus similar to that seen in subjects 2 and 3. Subject 4 exhibits strong positive maxima for right finger conditions which lies anterior and posterior to the central sulcus. A single equivalent dipole was computed for the right index and middle finger and the left middle finger conditions for this subject for the extracted potential maps using the 3 concentric sphere model. A radially oriented source was recovered for the right middle finger condition located within 2 mm of the central sulcus, and tangentially oriented sources were recovered for the left middle and right index finger conditions located within 3 and 2 mm of the central sulcus, respectively. The radial source may arise from a generator situated in the anterior or posterior crown of the central sulcus, and the tangential sources from a generator in the posterior bank of the central sulcus (Allison 1987; Desmedt et al. 1987). Several local maxima in the deblurred cortical potential pattern for the left middle finger response for subject 4 are observed over the posterior cortex; these may be due to spurious spatial noise in the scalp data which have been amplified by the deblurring technique. As described in Methods above, the deblurring technique can be sensitive to spatial noise in the scalp data. More work is underway to address this issue.

The stability of deblurred potentials was examined

across independent samples for all subjects for each somatosensory condition. The variability across samples was measured by finding the standard deviation of potential values at each cortical point over 3 independent samples of data (each 100 sec of recording for each SEP stimulus condition), and then calculating the mean of these standard deviations. This number was then expressed as a percentage of the within-sample variability, which was calculated by finding the mean range in potential values for each sample. These results (given in Table I) show that the across-sample variability was between 5.1 and 11.2% of the within-sample variability, which indicates that the deblurring procedure is stable.

The spatially enhanced scalp data presented above had been sampled with an inter-electrode spacing of 2.25 cm. The viability of the deblurring method was also examined using sparser scalp montages. The top row of Fig. 11 illustrates the effect of decreasing the number of recording sites on the 14.92 Hz SEP for subject 2. The recorded 124 channels were de-sampled and mapped for 18, 31, 64 and the entire 124 channels. A minor change in overall topography is observed with a decreasing number of electrodes for the linked-mastoid data. The location of the maximum is shifted in a posterior direction as a denser montage is used. Error in localization of the extrema resulting from a more sparsely populated montage was estimated for all subjects and conditions for 64, 31 and 18 channels. The error measurement was estimated in degrees as the angle between two vectors:

$$\Phi = (\overrightarrow{C_{bfs}P_{124_{\max}}}) \cdot (\overrightarrow{C_{bfs}P_{\text{de-sampled}_{\max}}})$$

where C_{bfs} is the center of the sphere best fit to 124 electrode coordinates; $P_{124_{\max}}$ is the location of the electrode for which the maximal electrical activity was recorded; and $P_{\text{de-sampled}_{\max}}$ is the location of the maximum within the 64-, 31- or 18-channel data set. The error decreases with better localization of the maximum. The error measurement was converted from degrees into centimeters by computing the distance between extrema points which were snapped to the best fitting sphere. For the 64-channel montage, the mean and standard deviation of the error of localization is $15.3^\circ (\pm 10.2)$ or 2.5 cm (± 1.7). For the 31-channel montage, the same mean and standard deviation were derived, because in all cases the maximum occurred at the same electrode common to both the 64-

Fig. 5. The same averages illustrated in Fig. 4 after the harmonic frequency extraction method has been applied.

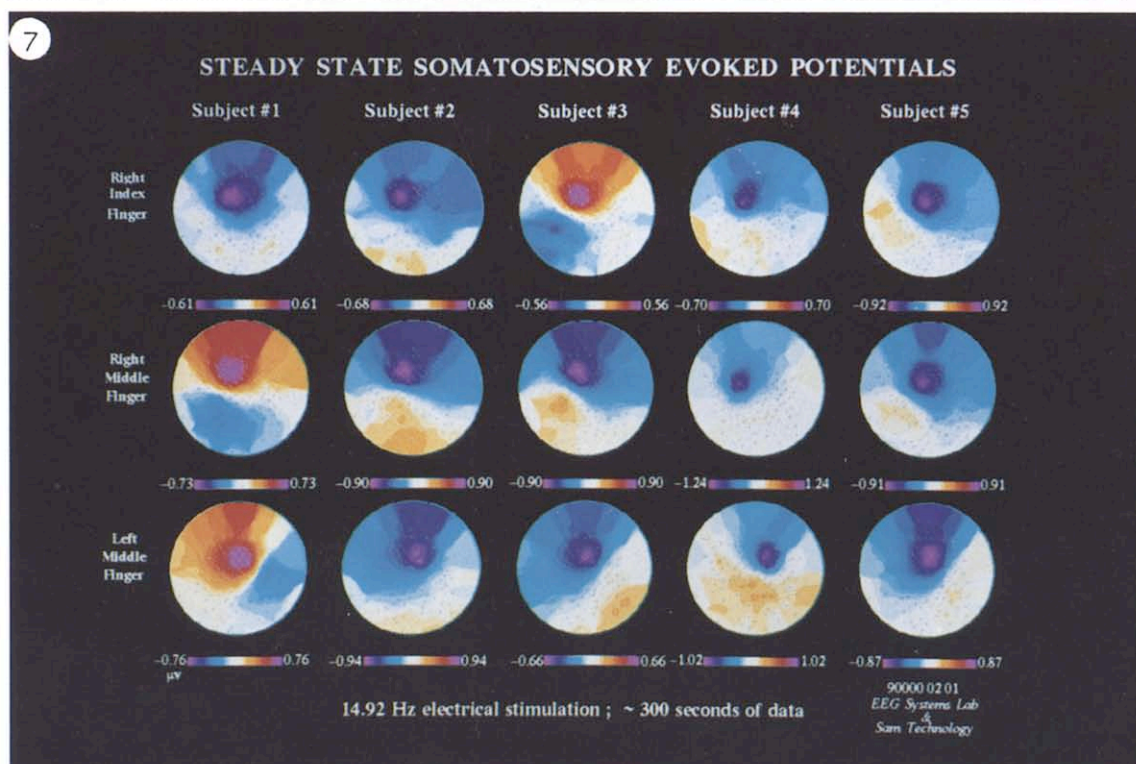
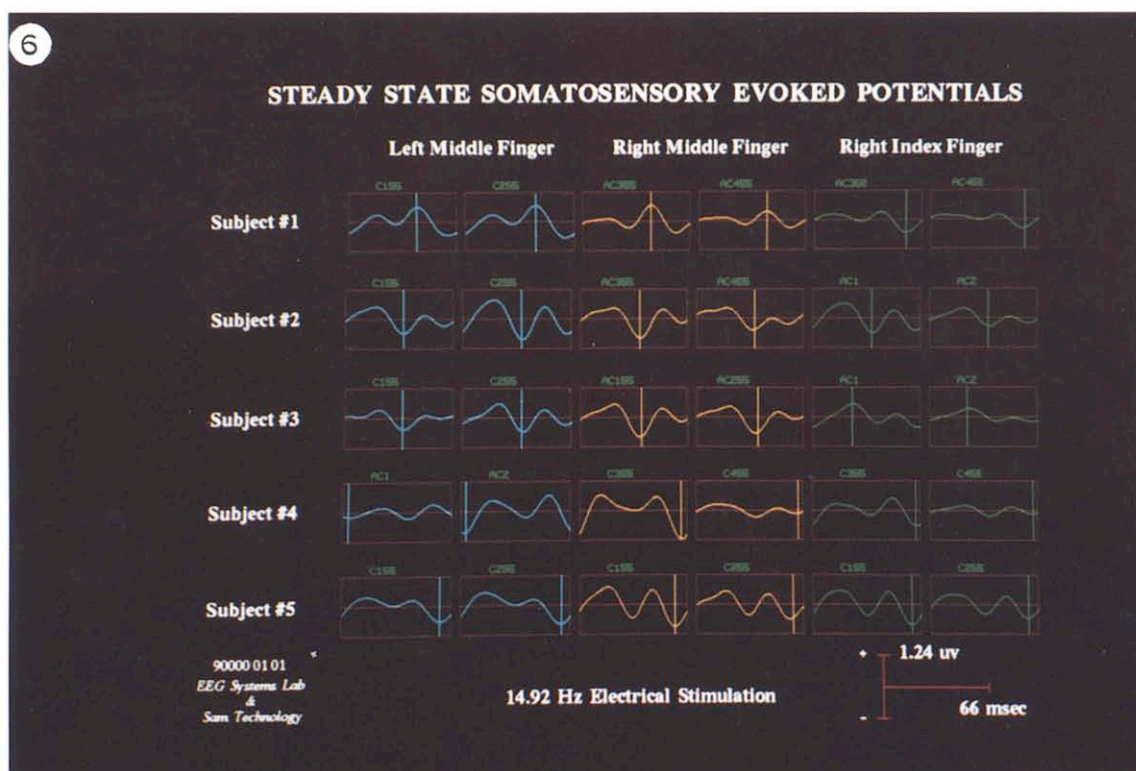


Fig. 6. The 14.92 Hz steady-state SEPs of 5 healthy subjects after the frequency extraction method has been applied. For each somatosensory condition, SEPs for the channel exhibiting the largest peak amplitude and SEPs for its homologous channel are shown. The left column is the left middle finger response, the middle column is right middle finger response, and the right column is the right index finger response. The vertical line indicates the phase within the steady-state cycle at which maximal global energy occurred for each condition and each subject.

Fig. 7. Traditional 2-D topographical maps of steady-state SEPs, referenced to linked mastoids, for all 5 healthy subjects. Maps were computed from 124 channels of data extracted at the phase within the steady-state cycle which exhibited maximum global energy. Since the maximum energy criterion was used for phase selection, the topographies for the right index finger response for subject 3 and the right and left middle finger responses for subject 1 exhibit a polarity inversion opposite that in the other maps. All maps are individually scaled; the values shown on the color bars are in units of microvolts.

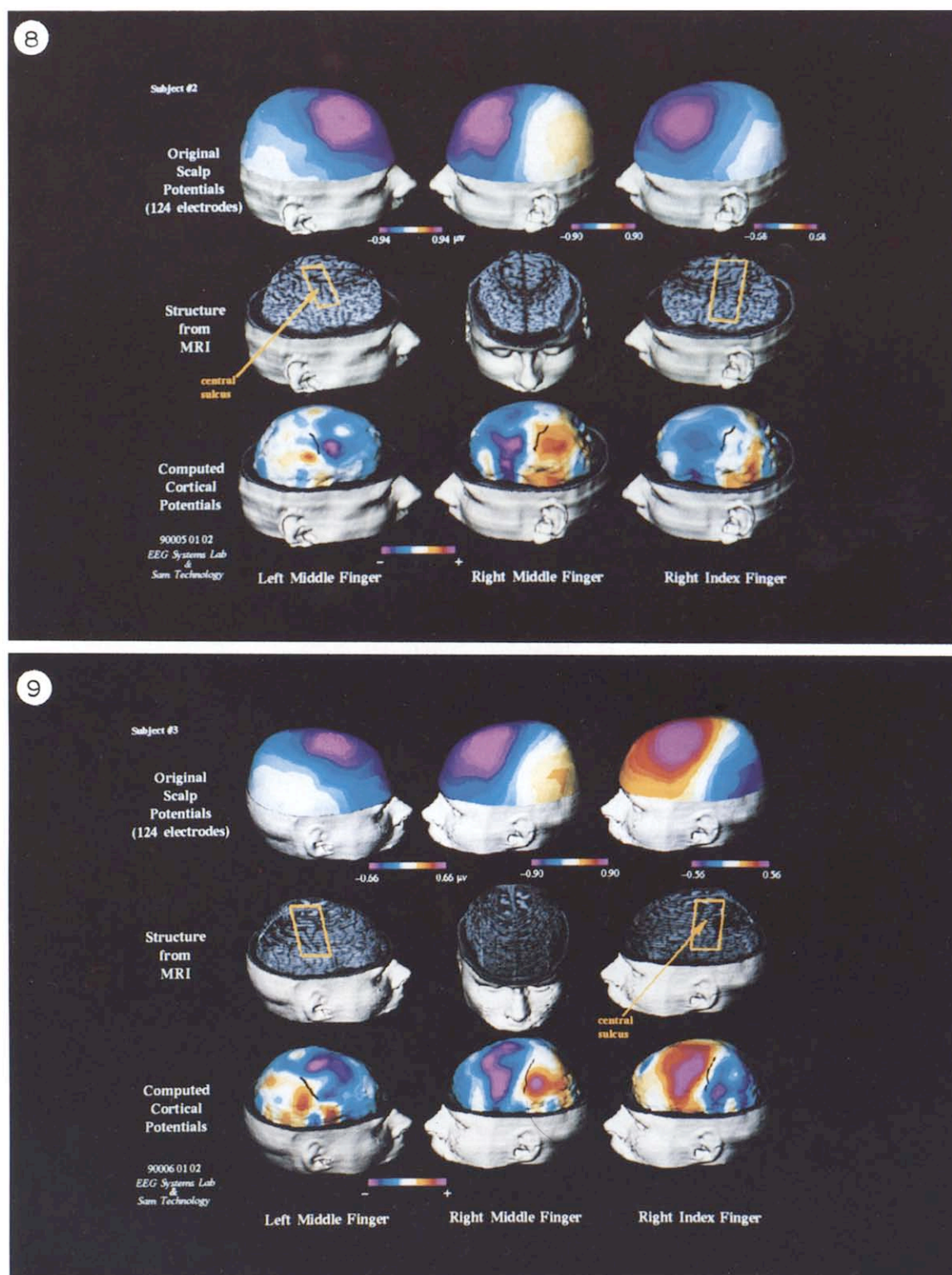


Fig. 8. Scalp and computed cortical steady-state SEPs for subject 2 (top and bottom rows, respectively). The left column is the left middle finger response; the middle and right columns are the right middle and index finger responses. All maps are individually scaled. The middle row displays a coarse image of subject 2's cortical anatomy obtained by stacking consecutive horizontal MR images. A yellow box delimits the pre- and post-central gyral regions. The black lines superimposed on the computed cortical potential image trace the individual's central sulcus. The computed cortical potentials illustrated in this figure exhibit enhanced spatial detail in comparison to the scalp potentials. The maximum and minimum computed potential foci were located on either side of the central sulcus.

Fig. 9. Scalp and computed cortical SEPs for subject 3 (top and bottom rows, respectively). Other details are as in Fig. 8.

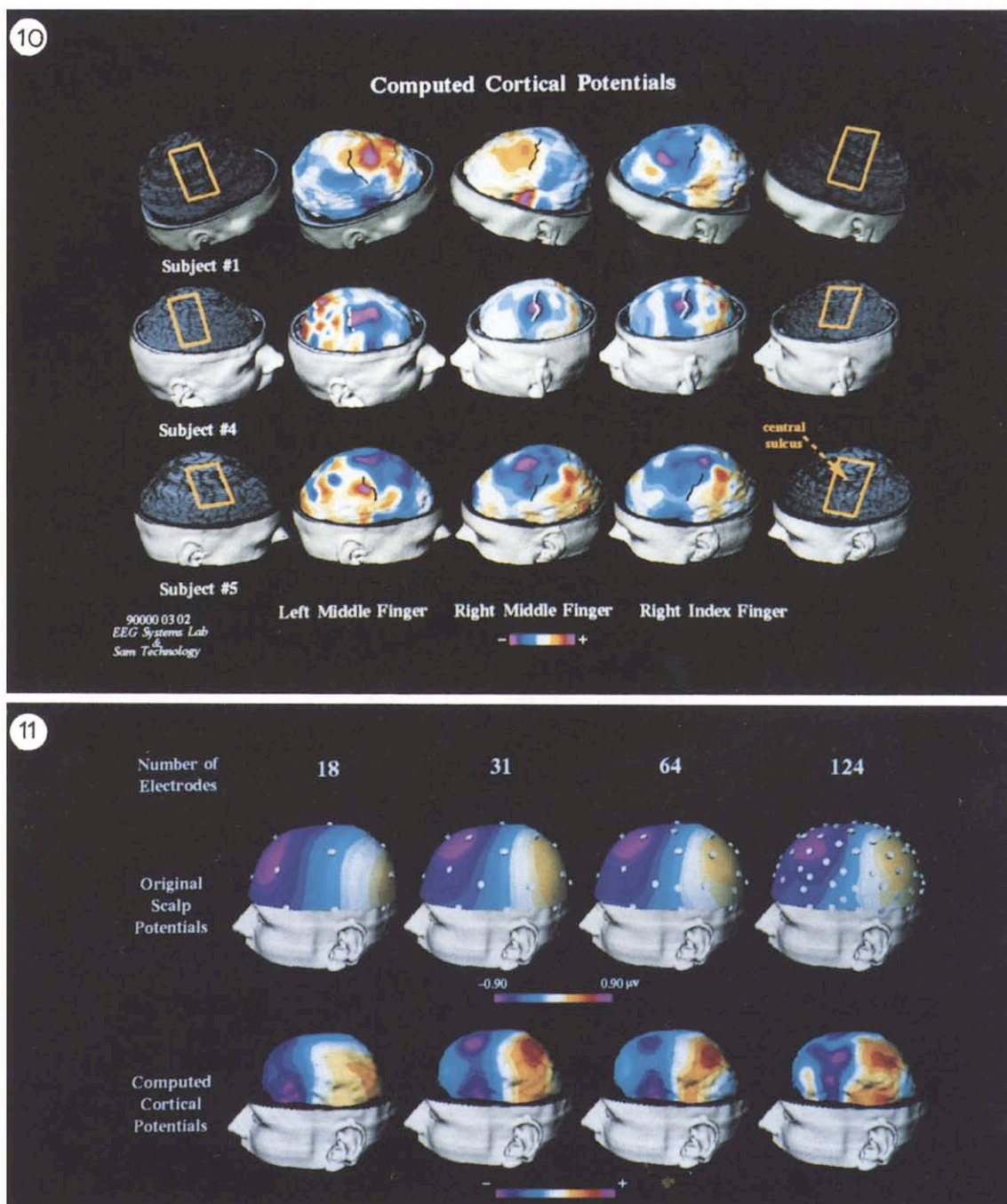


Fig. 10. Computed cortical steady-state SEPs for subjects 1, 4, and 5. Each row illustrates the left middle finger, right middle finger, and the right index finger response for an individual subject along with an image of the subject's cortical anatomy derived from MRI. For subject 4, the black lines superimposed on the computed cortical potential images which trace the subject's central sulcus are highlighted in white to improve visibility. Other details are as in Fig. 8.

Fig. 11. The effect of an increasing number of recording sites on the scalp-recorded (linked-mastoid reference) and computed cortical steady-state SEP topographic maps. SEPs were elicited by 14.92 Hz electrical stimulation of the right middle finger (same data as middle column of Fig. 8). The top row illustrates the effect of down-sampling the 124-channel scalp data to 64, 31 and 18 channels; the bottom row shows the corresponding computed cortical potentials. The white dots shown in images in the top row indicate scalp EEG recording sites. Other than a posterior shift in the location of the maximum, there is a relatively minor change in topography of the linked-mastoid potentials as the number of electrodes is increased. By contrast, the detailed topography of the computed cortical potentials changes dramatically as the number of electrodes increases from 18 to 124.

and 31-channel montages. With an 18-channel montage, the mean and standard deviation of the error of localization was $28.4^\circ (\pm 10.3)$ or $4.6 \text{ cm} (\pm 1.7)$. The bottom row of Fig. 11 illustrates the effect of spatial sampling at the scalp on deblurring results for the same data. The decreases in the number of electrodes from 124 to 64 and from 31 to 18 are each associated with a marked loss of spatial information.

(C) Comparison of deblurring results with subdural grid recordings

An initial empirical validation of the deblurring method was performed by comparing, for two patients, EPs recorded from a 64-channel grid over the somatosensory cortex to deblurred EPs recorded from the scalp prior to surgery. Cortical EEGs were recorded from electrodes (8×8 , each contact 1 cm apart, referenced to a skull screw near Cz) placed directly on the surface of the brain as part of the diagnostic evaluation of two patients with severe epilepsy who were candidates for neurosurgical treatment of their seizures. Because the patient's head must be wrapped in bandages at all times for sterility, scalp recordings could not be performed while the subdural grid is in place. (In any case, current shunts created by the skull defects associated with the lifting of a bone flap would be expected to distort the topography of any SEPs recorded at the scalp after grid placement.) Thus, in order to compare the cortical SEPs estimated by the deblurring method with the actual measured cortical EPs, a scalp SEP recording was made several days before grid implantation. In order to compare topographic patterns of cortical grid data and deblurred scalp data, all data sets were registered to the MRI coordinate system. Since grid data were referenced to a skull screw at Cz and scalp data were referenced to mathematically linked mastoids, it was necessary to remove the reference effect to compare the data sets. This was accomplished by converting the data to z scores.

Patient 1 was a 21-year-old woman with pharmacologically intractable seizures originating in the left hemisphere and right-hemisphere dominance for handedness and speech (as determined by the Wada test). Somatosensory stimulation of all 5 fingers of the right hand produced cortical evoked potentials which were almost identical in topography and showed an abnormally large response which is known to occur for some epileptics (referred to as "giant SEP," e.g., Shibasaki et al. 1990). The SEPs recorded from the cortical grid for the 5 fingers were averaged together, as were the scalp-recorded SEPs, and the deblurring method were applied to the averaged scalp data.

The original scalp potential topography, the deblurred (computed cortical potential) topography, and

the topography of potentials recorded directly from the subdural grid are shown in Fig. 12. To facilitate comparison of cortical grid and deblurred data, the grid data were spatially low-pass filtered to eliminate spatial frequencies higher than those which could be resolved with the spatial sampling frequency set by the inter-electrode spacing on the scalp. A description of the spatial filter is given in Eqn. 4. For illustrative purposes, Fig. 12 also shows scalp potentials spatially enhanced with a 3-D spline Laplacian derivation using a realistic head-shape model derived from the measured electrode positions (cf., Gevins et al. 1991; Le et al. 1994). The grid potential map exhibited a single peak over the same region of cortex which elicited sensation in the fingers upon direct electrical stimulation. The deblurred potentials show a localized peak in the same area with a polarity reversal towards the midline which closely approximates the grid potential pattern. In contrast, the original scalp data exhibit a much broader single peak in the mid-parietal area of the left hemisphere. A mathematical comparison between the grid and deblurred data was not performed since the interpretation of the results could be skewed by a grid-MRI alignment which was based upon only a surgical photograph and sketch and a post-implant skull radiograph. However, it is obvious from visual comparison of the grid, deblurred and scalp topographies that the deblurring method successfully improved SEP spatial detail and reduced the blur distortion.

The stability of the deblurred potentials across independent samples and for different conductivity ratios was computed for each of the 5 individual fingers. These results showed that the across-sample variability was only 4.2% of the within-sample variability, which further indicates that the deblurring procedure is stable. Deblurring calculations were also performed using values of the scalp/skull and brain/skull conductivity ratio at a range of values varying $\pm 50\%$ from the standard value of 80. Results showed that different conductivity ratios produced gradual differences in the exact size of active regions and in the finer detail but did not dramatically change the overall pattern of activity (Le and Gevins 1993). (The optimal fit of conductivity ratios to the recorded data could not be

TABLE 1

Variability of deblurred cortical potentials (%).

Subject	Left middle	Right middle	Right index
1	6.539	5.139	8.861
2	6.070	8.919	9.885
3	11.294	6.762	9.594
4	5.615	6.720	9.390
5	9.500	7.500	6.515

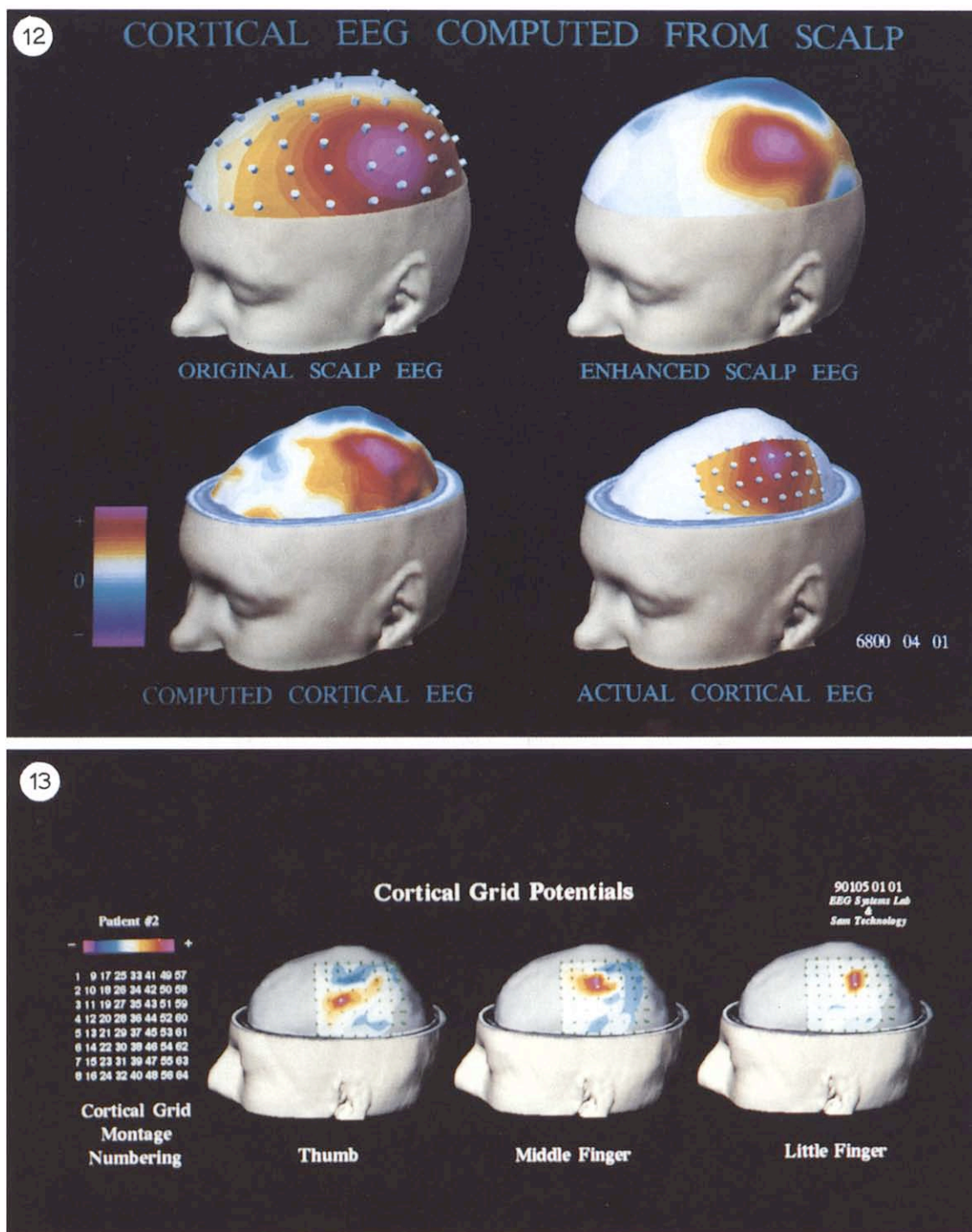


Fig. 12. The original scalp-recorded steady-state SEPs, the 3-D spline Laplacian derivation SEPs (labeled "enhanced scalp EEG"), the deblurred SEPs and SEPs subsequently recorded with a subdural grid for patient 1. The upper left figure illustrates the original SEP map on the scalp surface, and the upper right figure shows the Laplacian derivation SEPs. The small white disks on the scalp surface demarcate the recording electrodes. The lower left figure shows the deblurred potentials, and the lower right figure illustrates the SEPs recorded directly on the cortical surface, with the small disks representing the recording electrodes of the cortical grid. The computed cortical potentials exhibit more spatial detail than the scalp map, and closely approximate the cortical potential pattern. In the harmonic analysis of the giant SEP data for patient 1, only the fundamental component was included in the frequency extraction technique. A spatially varying Gaussian low-pass filter described by Eq.(4) has been applied to the grid data to approximate the spatial sampling of the scalp EEG montage.

Fig. 13. Subdural grid recording of SEPs elicited by electrical stimulation of the thumb, middle and little finger of patient 2 at a latency of 31 msec are shown. The numbering of the cortical grid montage is shown at the left. The data have been converted to z scores across each grid; the values shown for the color bars for the thumb, middle and little finger responses are $+/-5.04$, 4.18 , and 5.50 z units, respectively. The potential topography elicited by stimulation of the little finger is focused at electrode sites posterior and medial to the area of activation observed for the middle finger and thumb; this is consistent with the organization of the somatosensory homunculus.

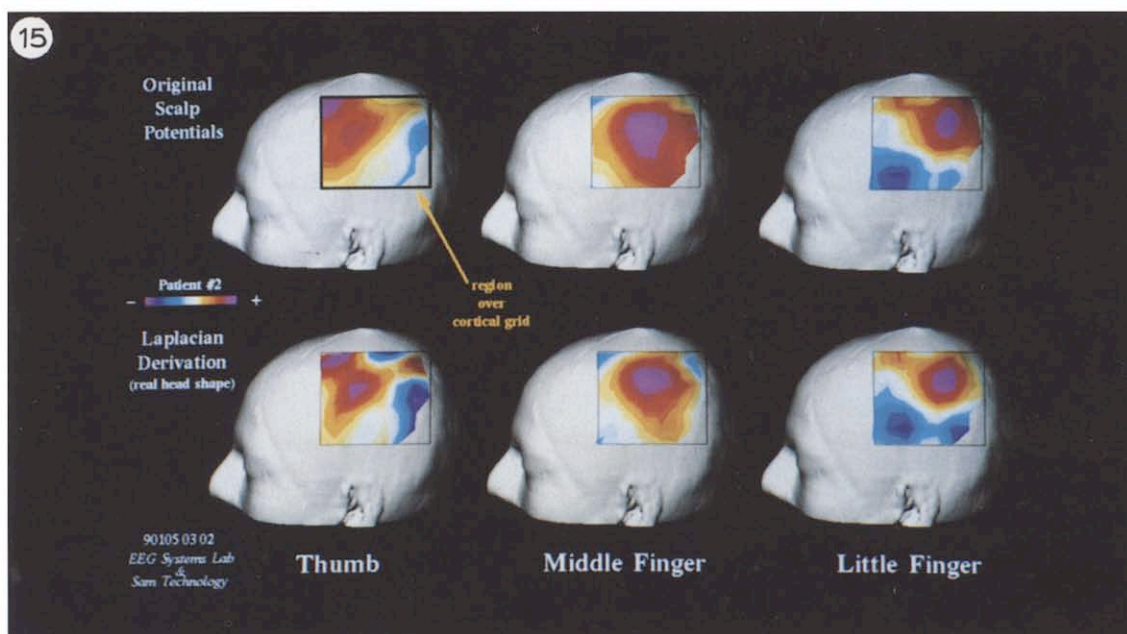
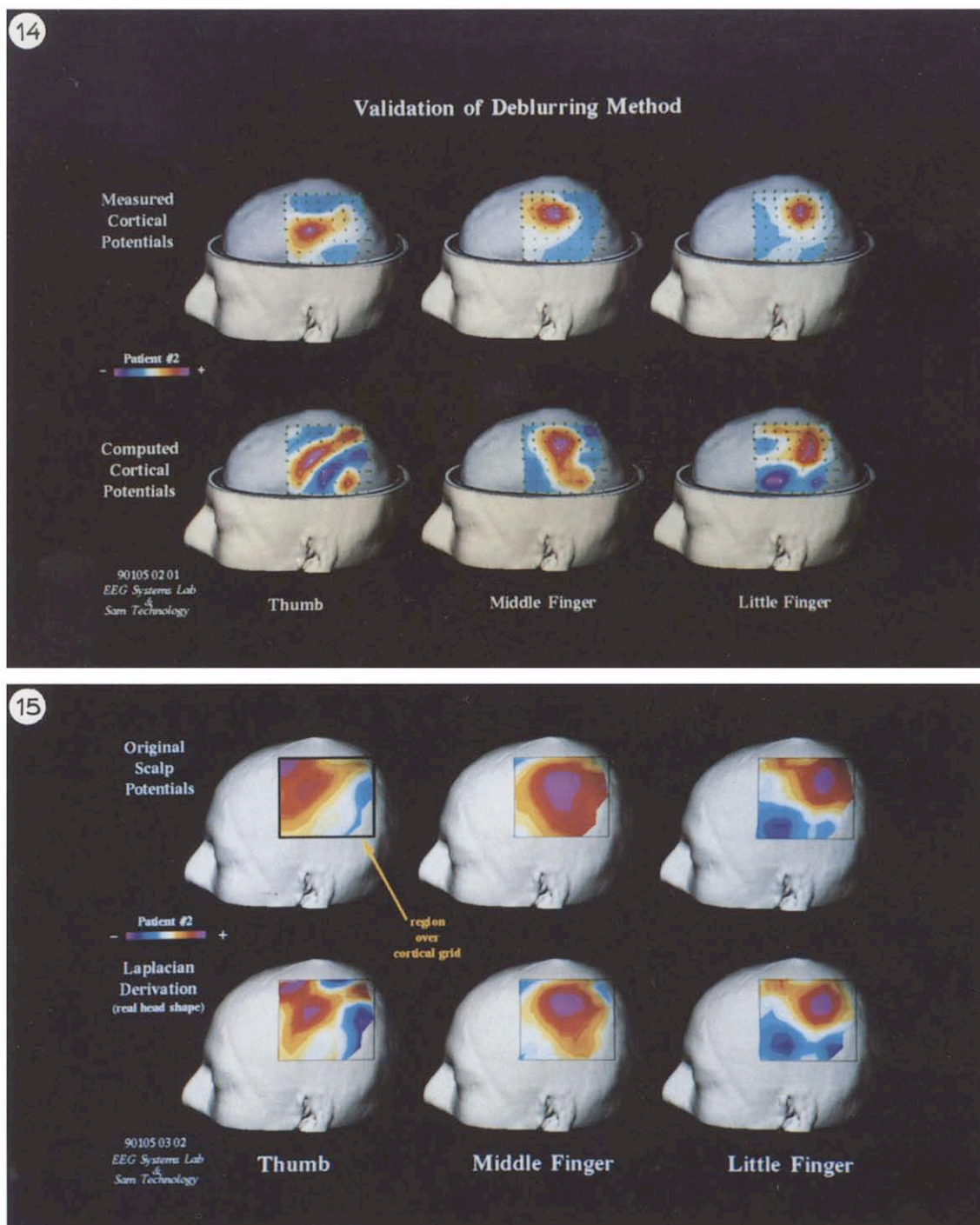


Fig. 14. Comparison of computed cortical SEPs with SEPs measured with a subdural grid for patient 2. The top row shows the z scores of grid SEPs elicited by electrical stimulation of the thumb, middle and little finger of patient 2 (same data as Fig. 3 but a Gaussian spatial low-pass filter, described by Eqn. (4), has been applied to approximate the spatial sampling of the scalp EEG montage). The color scale for the smoothed cortical z score values for the thumb, middle and little finger responses were ± 2.23 , 2.17 and 2.62 z units, respectively. The bottom row shows the corresponding computed cortical SEPs. The locations of grid electrodes are shown as dots to facilitate comparison with the grid recording. The color scale for the computed cortical z scores values for the thumb, middle and little finger responses were ± 2.28 , 2.38 and 2.51, respectively. The location of the large maximum of the computed cortical potentials for the thumb, middle and little finger parallels that in the grid recordings. The computed cortical potentials differ from the grid recordings at the bottom of the recording array, an effect visible in the scalp data (Fig. 15) whose origin is at present unknown.

Fig. 15. The scalp SEPs and 3-D spline Laplacian SEPs for the thumb, middle, and little finger for patient 2. Only the data directly over the cortical grid are shown to facilitate comparison with Fig. 14. All maps are individually scaled. The values shown on the color bar for thumb, middle and little finger scalp potentials are 1.21, 0.76, and 0.65 μV , respectively; the values shown on the color bar for thumb, middle and little finger Laplacian derivations are 0.129, 0.157, and 0.125 $\mu\text{V}/\text{cm}^2$, respectively.

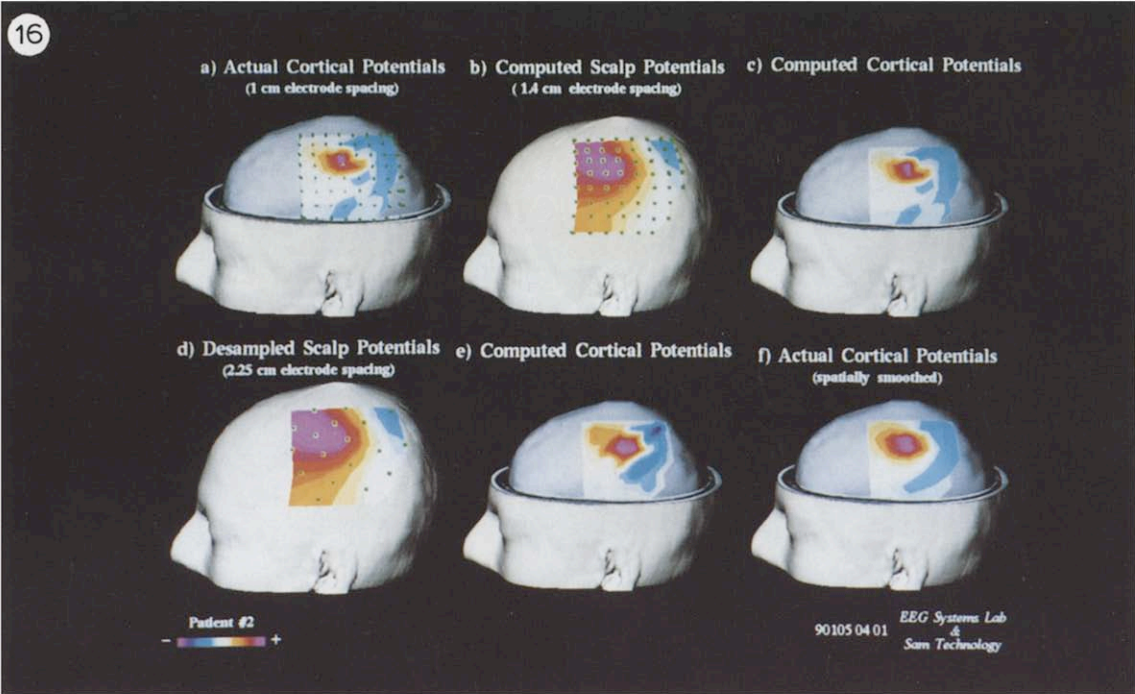


Fig. 16. The effect of scalp interelectrode spacing on computed cortical potentials obtained with the deblurring method. a: the actual cortical SEPs, recorded with a subdural grid, in response to electrical stimulation of the right middle finger (same data as Fig. 13, middle). b: the forward solution SEPs at the scalp computed from the data shown in (a) using an 1.4 cm scalp inter-electrode spacing corresponding to about 250 electrodes spread evenly over the head. (c) The cortical potentials computed from the data shown in (b). (d) The scalp data shown in (b) downsampled to an inter-electrode spacing of 2.25 cm corresponding to about 120 electrodes spread over the head. e: the cortical potentials computed from the scalp data of (d). f: the actual cortical SEPs of (a) spatially low-pass filtered to maintain a spatial frequency resolution consistent with the scalp inter-electrode spacing of 2.25 cm. This figure suggests that a denser spatial sampling at the scalp (about 250 electrodes) will provide computed cortical data with better spatial resolution (compare maps a and e). It also demonstrates that it is appropriate to apply a spatial low-pass filter to the grid data to fairly compare those data with computed cortical data obtained with a montage which is sparser than that of the grid as was done in Figs. 12 and 14 (compare maps e and f).

estimated because different stimulus intensities were used for scalp and grid recordings and the accuracy of grid-MRI alignment was uncertain.)

Patient 2 was a 20-year-old woman with pharmacologically intractable seizures originating in the left hemisphere and right hemisphere dominance for handedness and speech (as determined by the Wada test). Somatosensory stimulation was performed as described above except that only two 100 sec blocks were recorded for each stimulus condition. The alignment of the cortical grid with the MRIs recorded prior to surgery was performed based on information from a skull radiograph of the implanted grid, surgical photograph

and sketch, and the neurosurgeon's comments. To facilitate comparison of the grid and deblurred potentials, the finite element model used for deblurring was constructed as a small rectangular patch compatible with the cortical grid montage rather than as a model of the entire head.

For patient 2, electrical stimulation of each finger of the right hand produced distinctly different topographies. Fig. 13 illustrates the z scores of grid potentials extracted for the thumb, middle finger, and little finger at a latency of 31 msec post stimulus. The green dots represent the cortical grid electrode positions which

TABLE II
Normalized root mean square error.

Finger	Thumb	Middle	Little
Grid-deblur	0.967	0.784	0.788
Grid-scalp	1.638	1.530	1.397

TABLE III
Angle of localization error (degrees).

Finger	Thumb	Middle	Little
Grid-deblur	0.00	0.00	12.30
Grid-scalp	32.62	7.81	10.86

are numbered in a system shown on the left side of the figure. Consistent with the organization of somatosensory homunculus, the potential topography elicited by stimulation of the little finger is focused at electrode sites posterior and medial to the activation observed for the middle finger and thumb. The localizations from grid SEPs were consistent with the results from direct cortical stimulation which were performed to localize the functional cortical regions. Stimulation of grid electrodes 21 and 29 produced extension of the thumb; stimulation of electrodes 35 and 36 produced extension of the little finger. These electrode sites recorded the strongest responses to electrical stimulation of the thumb and little finger, respectively. Stimulation of electrodes 28 and 30 elicited movement of all 5 fingers; stimulation of 43 and 44 produced sensation in the fingers as well as movement.

In order to visually compare actual cortical grid data sampled at 1 cm electrode spacing with deblurred data computed from scalp data sampled at 2.25 cm spacing, a low-pass spatial filter (described in Eqn. 4) was applied to the z scores of grid data (illustrated in Fig. 13) to eliminate spatial frequencies which could not possibly be recovered with the interelectrode spacing at the scalp. The z scores of the cortical data are shown in the top row of Fig. 14 for the 3 somatosensory conditions; the z scores of deblurred (computed cortical) potentials (extracted at the same latency as the cortical grid potentials, 31 msec) are illustrated in the bottom row. The original scalp potentials, and for illustrative purposes the 3-D spline Laplacian, are shown in Fig. 15. An evaluation of how well the scalp and deblurred potentials approximate the cortical grid data was performed by computing the normalized RMS errors comparing scalp and deblurred z scores at 64 points on the scalp or cortical surface to the 64 smoothed cortical z scores. The normalized RMS error was computed as:

$$\text{RMSE} = \frac{\sqrt{\sum_{i=1}^N (V_{g_i} - V_{e_i})^2}}{\sqrt{\sum_{i=1}^N V_{g_i}^2}}$$

where N is the number of grid electrodes, V_g is the z score value of the grid electrode, and V_e is the z score value of either the scalp or deblurred data.

Another evaluation was performed to quantify the error on the localization of the extrema comparing the location of the scalp and deblurred z score extrema with the actual grid z score extrema for the two data sets. The error of localization of the maximum is the angle between two vectors:

$$\Phi = (\overline{C_{bfs} P_{g_{\max}}}) \cdot (\overline{C_{bfs} P_{e_{\max}}})$$

where C_{bfs} is the point in 3-D space of the center of the sphere best fit to the cortical grid coordinates; $P_{g_{\max}}$ is the location of the grid electrode for which the maximal electrical activity was recorded; and $P_{e_{\max}}$ is the location of the maximum estimated by either the deblurred or scalp data over the same area. This error becomes smaller as the data localize the maximum better.

The results of the two evaluation tests are given in Tables II and III. The results in Table III show that the deblurring procedure accurately estimated the grid maximum in 2 of 3 cases, and in the third case the localization error was 12.30°. The errors in the localization of the maximum for the scalp data were larger for the thumb than the middle and little finger, and were never zero as was obtained with the deblurring procedure. These results suggest that the deblurring procedure is valid and that it provides an accurate topographical localization of the dominant cortical potential peak. The RMS errors reported in Table II for the deblurred data were consistently smaller than the scalp data. However, the magnitude of error reported in Table II (resulting from enhanced negative peaks in the deblurred data not observed in the cortical grid data) may be due to enhancement of spatial noise present in the scalp data. This points to the importance of using data with a high signal-to-noise ratio and/or developing methods to reduce spatial noise when applying spatial deconvolution techniques such as deblurring.

Utilizing the deblurring technique, different cortical areas devoted to somatosensory functions of the thumb, middle and little fingers could be distinguished and resolved from scalp recordings sampled at 2.25 cm. The estimated cortical potentials for the thumb, middle and little finger exhibited distinctly different spatial patterns similar to the patterns recorded directly from a dense cortical grid montage with 1 cm inter-electrode spacings. However, due to higher spatial sampling, the cortical grid data exhibited sharper spatial features than the resulting deblurred (estimated cortical) data. To make a fair comparison of the deblurring and cortical grid data, a low-pass spatial filter was applied to the data recorded directly from the cortical grid. To check the validity of the spatial filtering approach applied in this study as well as to determine what scalp montage spacing should be used for future validation studies such that the corresponding deblurred data can be directly compared to measured cortical data without use of the spatial filtering technique, a simple simulation was performed. In this simulation, the 64 cortical grid points were radially projected onto the scalp surface, and the scalp forward solution was computed using the finite element model for 64 measured cortical potentials recorded on the 1 cm cortical grid spacing (illustrated in Fig. 16a). The resulting scalp data are

shown in Fig. 16b. This scalp forward solution was next de-sampled to a 2.25 cm inter-electrode spacing comparable to the 124-electrode montage used in our study (Fig. 16d). Then, the estimated cortical data (illustrated in Fig. 16e) were derived using the de-sampled scalp data and the same finite element model. Finally, the original cortical data were smoothed by a low-pass spatial filter (illustrated in Fig. 16f) and were compared with the deblurred data in Fig. 16e. A good match in patterns between these two maps is found. This suggests that it is appropriate to apply a low-pass spatial filter to densely sampled grid data to compensate for the fact that a sparser scalp electrode montage was used. It is evident that there is less spatial detail in Fig. 16e when it is compared to Fig. 16a. This indicates that a denser scalp montage should be used in future deblurring validation studies.

Discussion

Traditionally, EEG maps have been 2-dimensional planar representations of 16, 19 or 32 channels. This paper has described methods for recording 124 scalp channels, registering EEG data with MRIs, and spatially enhancing these data with a mathematical deblurring technique for calculating potentials near the superficial cortical surface using a realistic MRI-based model of a subject's head. We have shown that increasingly greater spatial detail of scalp potential fields is obtained with a large number of recording electrodes. Furthermore, we have demonstrated that the spatial resolution of brain activity can be greatly enhanced by correcting for the blur distortion which occurs as cortical potentials pass through conducting volumes of the skull and scalp. We have demonstrated visualization of scalp and deblurred EP potential maps on a realistic 3-D anatomical head model viewed from different view points. Comparison of the more traditional 2-D maps illustrated in Fig. 7 with the 3-D maps in Figs. 8–10 demonstrates the striking difference in spatial and anatomical detail provided by this technique. The initial results presented in this paper, which show the individual variability among 5 subjects for stimulation in 3 somatosensory conditions, are quite promising and suggest that the coupling of high-resolution, 3-D deblurred evoked potential mapping with anatomical imaging techniques such as MRI makes it possible to visualize an approximation of electrical activity near the superficial cortical surface. At the expense of recording and analyzing an MRI from each subject and performing some additional computation, the deblurring method accounts for variations in volume conduction distortion due to local variations in skull thickness.

The comparison in two patients of deblurred scalp-recorded data with cortical grid data suggests that the deblurring procedure provides a more accurate localization of cortical activity than has previously been possible.

Unlike other methods which estimate cortical potentials or currents (e.g., Nicholas and Deloche 1976; Freeman 1980; Hill et al. 1988; Sidman et al. 1989, 1992), deblurring is a true “downward continuation” method in that the cortical potential distribution is derived without prior knowledge or assumptions about the generating sources. Also, deblurring uses a realistic model of the head shape and local tissue thicknesses, rather than assuming that the scalp, skull and brain are spherically shaped. Although deblurring appears to be effective in producing a more focal potential pattern near the cortical surface, it is not a source localization method. An inferential process is required for the identification of electrical generators within the brain because ambiguities exist in the cortical potential patterns. Source localization techniques such as multiple dipole modeling (Scherg and Von Cramon 1985; Scherg 1989) or 3-D spatial filters and beam forming (Mosher et al. 1992; Van Veen et al. 1992), combined with source constraints based on data from functional MRI recordings, may enable visualization of the distributed neuroelectrical activity underlying brain sources. Further research will determine whether deblurring would be a useful component of such source modeling.

Based on these encouraging preliminary results, it appears worthwhile to further develop high-resolution EEG in general and the deblurring method in particular. More work is needed to produce a better conducting model of the head, including more accurate estimates of conductivity for the tissues modeled, as well as an account of the important sources of anisotropy, such as the presence of higher-conductivity diploes and sutures in the skull. Another important area of research is assessing the effect of spatial noise on deblurring to determine the optimal spatial filtering required for different types of data.

Portions of the material in this paper were first presented as the President's Invited Lecture at the 1990 annual meeting of the American Society for Neuroscience.

Supported by the National Institute of Mental Health, the National Institute of Neurological Diseases and Stroke, the Air Force Office of Scientific Research, the Office of Naval Research and the National Science Foundation.

Access to neurosurgery patients was provided by the Northern California Comprehensive Epilepsy Center at the University of California San Francisco, Dr. Kenneth Laxer, Director, and Dr. Nicholas Barbaro, Neurosurgeon. Major scientific contributions to this work were made by Drs. Steven Bressler and Brian Cutillo. Computer programming and additional technical assistance was provided by Jim Alexander, Heidi Basseler, George Blanco, Bryan Costales,

Deanna Dack, Kristen Jerger, Mark Levin, Frank Luo, Judy McLaughlin, Alisa Surkis, Lindsay Vurek and Michael Ward. Dr. Michael Smith helped rewrite the manuscript.

References

- Allison, T. Normal limits in the EP: age and sex differences. In: S. Butler, R. Paul and A.M. Halliday (Eds.), *Textbook of Clinical Neurophysiology*. Wiley, Chichester, 1987.
- Allison, T., McCarthy, G., Wood, C., Darcey, T., Spencer, D. and Williamson, P. Human cortical potentials evoked by stimulation of the median nerve. I. Cytoarchitectonic areas generating short-latency activity. *J. Neurophysiol.*, 1989a, 62: 604–710.
- Allison, T., McCarthy, G., Wood, C., Williamson, P. and Spencer, D. Human cortical potentials evoked by stimulation of the median nerve. II. Cytoarchitectonic areas generating long-latency activity. *J. Neurophysiol.*, 1989b, 62: 710–722.
- Belliveau, J.W., Kennedy, D.N., McKinty, R.C., Buchbinder, B.R., Weisskoff, R.M., Cohen, M.S., Vevea, J.M., Brady, T.J. and Rosen, B.R. Functional mapping of the human visual cortex by magnetic resonance imaging. *Science*, 1991, 254: 716–719.
- Delberghe, X., Mavrouidakis, N., Zegers de Beyl, D. and Brunko, E. The effect of stimulus frequency on post- and pre-central short-latency somatosensory evoked potentials (SEPs). *Electroenceph. clin. Neurophysiol.*, 1990, 77: 86–92.
- Desmedt, J. and Brunko, E. Functional organization of far-field and cortical components of somatosensory evoked potentials in normal adults. In: J. Desmedt (Ed.), *Progress in Clinical Neurophysiology* (Vol. 7). Karger, Basel, 1980: 27–50.
- Desmedt, J., Nguyen, T.H. and Bourguet, M. Bit-mapped color imaging of human evoked potentials with reference to the N20, P22, P27 and N30 somatosensory responses. *Electroenceph. clin. Neurophysiol.*, 1987, 68: 1–19.
- Freeman, W.J. Use of spatial deconvolution to compensate for distortion of EEG by volume conduction. *IEEE Trans. Biomed. Eng.*, 1980, 27: 421–429.
- Gevins, A.S. Obstacles to progress. In: A.S. Gevins and A. Rémond (Eds.), *Methods of Analysis of Brain Electrical and Magnetic Signals. Handbook of Electroencephalography and Clinical Neurophysiology* (Revised), Vol. 1. Elsevier, Amsterdam, 1987: 665–673.
- Gevins, A.S. Recent advances in neurocognitive pattern analysis. In: E. Başar (Ed.), *Dynamics of Sensory and Cognitive Processing of the Brain*. Springer, Heidelberg, 1988: 88–102.
- Gevins, A. Dynamic functional topography of cognitive tasks. *Brain Topogr.*, 1989, 2: 37–56.
- Gevins, A. Dynamic patterns in multiple lead data. In: J. Rohrbaugh, R. Johnson and R. Parasuraman (Eds.), *Event-Related Brain Potentials: Basic Issues and Applications*. Oxford University Press, New York, 1990: 44–56.
- Gevins, A., Brickett, P., Costales, B., Le, J. and Reutter, B. Beyond topographic mapping: towards functional-anatomical imaging with 124-channel EEGs and 3-D MRIs. *Brain Topogr.*, 1990, 3: 53–64.
- Gevins, A., Le, J., Brickett, P., Reutter, B. and Desmond, J. Seeing through the skull: advanced EEGs use MRIs to accurately measure cortical activity from the scalp. *Brain Topogr.*, 1991, 4: 125–131.
- Hill, C.D., Kearfott, R.B. and Sidman, R.D. The inverse problem of electroencephalography using an imaging technique for simulating cortical surface data. In: R. Vichnevetsky, P. Borne and J. Vignes (Eds.), *Proc. 12th IMACS World Cong.*, Vol. 3, 1988: 735–738.
- Jasper, H.H. The ten–twenty electrode system of the International Federation. *Electroenceph. clin. Neurophysiol.*, 1958, 10: 371–375.
- Le, J. and Gevins, A.S. Method to reduce blur distortion from EEGs using a realistic head model. *IEEE Trans. Biomed. Eng.*, 1993, 40: 517–528.
- Le, J., Menon, V. and Gevins, A. Local estimate of surface Laplacian derivation on a realistically shaped scalp surface and its performance on noisy data. *Electroenceph. clin. Neurophysiol.*, 1994, in press.
- Lehmann, D. Spatial analysis of EEG and evoked potential data. In: F. Duffy (Ed.), *Topographic Mapping of Brain Electrical Activity*. Butterworth, Boston, MA, 1986: 143–168.
- Lüders, H., Dinner, D.S., Lesser, R.P. and Morris, H.H. Evoked potentials in cortical localization. *J. Clin. Neurophysiol.*, 1986, 3: 75–84.
- Mosher, J., Lewis, P. and Leahy, R. Multiple dipole modeling and localization from spatio-temporal MEG data. *IEEE Trans. Biomed. Eng.*, 1992, 39: 541–557.
- Nakamura, M., Nishida, S. and Shibasaki, H. Spectral properties of signal averaging and a novel technique for improving the signal-to-noise ratio. *J. Biomed. Eng.*, 1989, 11: 72–78.
- Namerow, N., Sciabassi, R. and Enns, N. Somatosensory responses to stimulus trains: normative data. *Electroenceph. clin. Neurophysiol.*, 1974, 37: 11–21.
- Nelder, J.A. and Mead, R. A simplex method for function minimization. *Comput. J.*, 1965, 7: 308–313.
- Nicholas, P. and Deloche, G. Convolution computer processing of the brain electrical image transmission. *Int. J. Bio-Med. Comput.*, 1976, 7: 143–159.
- Ogawa, S., Tank, D.W., Menon, R., Ellermann, J.M., Kim, S.-G., Merkle, H. and Ugurbil, K. Intrinsic signal changes accompanying sensory stimulation: functional brain mapping using MRI. *Proc. Nat. Acad. Sci. (USA)*, 1992, 89: 5951–5955.
- Ogawa, S., Menon, R., Tank, D., Kim, S., Merkle, H., Ellermann, J. and Ugurbil, K. Functional brain mapping by blood oxygenation level-dependent contrast magnetic resonance imaging. A comparison of signal characteristics with a biophysical model. *Biophys. J.*, 1993, 64: 803–812.
- Pratt, H., Politoske, D. and Starr, A. Mechanically and electrically evoked somatosensory potentials in humans: effects of stimulus presentation rate. *Electroenceph. clin. Neurophysiol.*, 1980, 49: 240–245.
- Regan, D. *Evoked Potentials in Psychology, Sensory Physiology and Clinical Medicine*. Chapman and Hall, London, 1972.
- Regan, D. *Human Brain Electrophysiology: Evoked Potentials and Evoked Magnetic Fields in Science and Medicine*. Elsevier, New York, 1989.
- Scherg, M. Fundamentals of dipole source potential analysis. In: M. Hoke, F. Grandori and G.L. Romani (Eds.), *Advances in Audiology*. Karger, Basel, 1989.
- Scherg, M. and Von Cramon, D. Two bilateral sources of the late AEP as identified by a spatio-temporal dipole model. *Electroenceph. clin. Neurophysiol.*, 1985, 62: 32–44.
- Sharbrough, F., Chatrian, G.E., Lesser, R.P., Lüders, H., Nuwer, M. and Picton, T.W. Guidelines for Standard Electrode Position Nomenclature. American Electroencephalographic Society, 1990.
- Shibasaki, H., Nakamura, M., Nishida, S., Kakigi, R. and Ikeda, A. Wave form decomposition of “giant SEP” and its computer model for scalp topography. *Electroenceph. clin. Neurophysiol.*, 1990, 77: 286–294.
- Sidman, R.D., Kearfott, R.B., Major, D.J., Hill, D.C., Ford, M.R., Smith, D.B., Lee, L. and Kramer, R. Development and application of mathematical techniques for the noninvasive localization of the sources of scalp-recorded electric potentials. In: J. Eisenfeld and D.S. Levine (Eds.), *IMACS Trans. Scientific Computing*, Vol. 5. Baltzer, Basel, 1989: 133–157.

- Sidman, R.D., Vincent, D.J., Smith, D.B. and Lee, L. Experimental tests of the cortical imaging technique – applications to the response to median nerve stimulation and the localization of epileptiform discharges. *IEEE Trans. Biomed. Eng.*, 1992, **BME-39**: 437–444.
- Strang, G. and Fix, G. *An Analysis of the Finite Element Method*. Prentice-Hall, Englewood Cliffs, NJ, 1973.
- Snyder, A. Steady-state vibration evoked potentials: description of technique and characterization of responses. *Electroenceph. clin. Neurophysiol.*, 1992, **84**: 257–268.
- Van Veen, B., Joseph, J. and Hecox, K. Localization of intra-cerebral sources of electrical activity via linearly constrained minimum variance spatial filtering. In: *IEEE 6th Signal Processing Workshop on Statistical Signal and Array Processing*, Victoria, BC, 1992: 526–529.